ISSN: 2414-1895 DOI: 10.6919/ICJE.202308_9(8).0021

# Analysis of Bias Characteristics of FY-4A Satellite AGRI Imager based on ARMS

Huan Yang, Xiaofang Liu*, Zhuohui Zhou

School of Computer Science and Engineering, Sichuan University of Science & Engineering, Yibin 644000, Sichuan, China

*Corresponding author Email: lxf1969@163.com

## Abstract

**Before assimilating the radiance of the geostationary imager into the assimilation system, correctly characterizing the bias can effectively improve the accuracy of numerical weather prediction. The ARMS fast radiative transfer model is used to simulate the brightness temperature of the AGRI infrared channel with the ECMWF reanalysis data ERA5 as input, and to characterize the deviation between the simulated brightness temperature and the observed brightness temperature under clear sky conditions (observed brightness temperature - simulated brightness temperature), which is AGRI The product is applied to prepare for assimilation provided. The results show that the deviations of each channel on land and sea are less than 2K and 1.5K respectively. Channels 11-13 have more pronounced deviation differences between land and sea than the rest of the channels. After fitting by linear regression, there is no obvious dependence of each channel on the scanning angle on the sea surface. All channels have a dependence on the observed brightness temperature.**

## Keywords

**Advanced Radiative Transfer Modeling System(ARMS); Fengyun-4A (FY-4A); Advanced Geostationary Radiation Imager(AGRI); Bias Feature Analysis.**

## 1. Introduction

In recent years, a new generation of geostationary meteorological satellites has developed rapidly, and geostationary meteorological satellite data are playing an increasingly important role in monitoring disastrous weather, air pollution, surface solar irradiance and assimilating data for numerical weather prediction[1]. The three-axis stabilized FY-4A satellite is the first in a series of China's new generation of geostationary weather satellites. It was launched on December 11, 2016 and officially delivered on September 25, 2017. It is located at 104.7°E above the equator and at an altitude of 35,786 kilometers. FY-4A is equipped with the Advanced Geostationary Radiation Imager[2] (Advanced Geostationary Radiation Imager, AGRI), the Interferometric Atmospheric Vertical Sounder[3] (Geostationary Interferometric Infrared Sounder, GIIRS) and the Lightning Imager[4] (Lightning Mapping Imager, LMI). AGRI is similar to the Himarari Imager on the Japanese satellite Himawari-8[5] and the Advanced Baseline Imager (ABI) on the US geostationary weather satellite[6]. Among them, AGRI launched a number of new products such as cloud liquid water, aerosol optical depth, surface temperature and convection induction, providing more complete applications and services.

Geostationary imager observations are applied to identify and track rapidly changing weather phenomena and infer quantitative products that are critical for weather services and timely forecasting applications. Visible, shortwave infrared, and thermal infrared radiation information detected by

ISSN: 2414-1895 DOI: 10.6919/ICJE.202308_9(8).0021

geostationary imagers can be used to retrieve cloud information such as optical thickness, effective particle radius, and cloud top properties[7]. Cloud attribute products are widely used in cloud process monitoring[8], rainfall probability inversion[9], disastrous weather forecast[10], etc. In addition to conventional applications, using machine learning methods, stationary infrared observations can be directly applied to the study of meteorological conditions, such as total precipitation[11], tropical thunderstorm[12], quantitative precipitation estimation[13], etc. What is more striking is that the research on radiation assimilation of geostationary infrared observations is gradually expanding and deepening from clear-sky observations to all-sky observations[14]. Ouellet[15] assimilated the water vapor-sensitive infrared brightness temperature observations of the Advanced Baseline Imager (ABI) into the data assimilation research test bench set data assimilation system, and found that not only in the 3D water distribution, but also in the cloud, temperature The wind field has also been improved. Yang[16] first assimilated the imager radiance data on a US geostationary weather satellite using an assimilation system with a hybrid 3D EnVar scheme, and had a certain significant positive impact on the convective permit forecast for Mexico. Other studies[17] have also shown that geosynchronous infrared radiation assimilation systems can have a positive impact on precipitation forecasting skills. In the past ten years, many achievements have been made in the assimilation of all-sky synchrotron infrared radiation, and significant progress has been made in the forecasting of rapidly changing weather systems (such as typhoons, precipitation, floods, etc.)[18].

For atmospheric parameter inversion and numerical weather prediction (Numerical Weather Prediction, NWP), the calibration and verification of geostationary imager observations are the first key conditions. Furthermore, it is critical to correctly quantify biases and errors before assimilating geostationary imager radiance rates into a data assimilation system, as biases between satellite observation information and background field data can reduce the accuracy of numerical weather prediction[19]. A common approach to assess the discrepancy between satellite observations and model simulations is to simulate brightness temperatures using reanalysis data and radiative transfer models[20].

So far, AGRI infrared channel bias assessment in selected areas has been studied based on assimilation of forecast model data from synoptic studies and radiative studies from ARMS[21]. However, there is no assessment of the bias characterization of AGRI infrared emissions based on FY-4A satellite observations and MODIS cloud mask products. In this paper, ARMS is used as the radiative transfer model, and the fifth-generation atmospheric reanalysis data set ERA5 of the European Center for Medium-Range Weather Forecasts (ECMWF) is used as the model input to obtain the deviation between observation and simulation, so as to characterize the selected The deviation of the AGRI infrared band of the FY-4A star in the Dinghai land area provides preparations for the application of AGRI products to the forecast model data assimilation.

## 2. Data and Method

### 2.1 Data Preprocessing

In this paper, the ERA5 data is used as the input data of the ARMS model, and the brightness temperature of the AGRI infrared channel is simulated; then the deviation is obtained by subtracting the simulated data from the AGRI observation data; finally, the deviation distribution is analyzed. Download the ERA5 data with a horizontal resolution of 0.1°×0.1° and a time resolution of 1h through the API interface. Because the spatial and temporal resolutions of ERA5 data and AGRI observation data are different, before the simulation, the ERA5 data is interpolated to the space-time grid of AGRI observation by bilinear interpolation in space and inverse weight interpolation in time. Since this paper focuses on the deviation analysis of the AGRI infrared channel under clear sky conditions, the MODIS cloud product is selected to perform cloud detection on the simulation results. The AGRI data and MODIS data in August 2018 were selected for screening, and the data with clouds and possible clouds in the AGRI data were eliminated, and then the deviation analysis with the simulation results was carried out.

ISSN: 2414-1895 DOI: 10.6919/ICJE.202308_9(8).0021

### 2.2 Method

The ARMS rapid transfer transfer model simulates the radiation observed by satellite sensors by solving the radiative transfer equation for the observed atmospheric conditions. The radiative transfer equation under clear-sky conditions is given by equation (1):

$$L^{Clr}(\nu,\theta)=[1-\varepsilon_S(\nu,\theta)]\tau_S^2(\nu,\theta)\int_{\tau_S}^{1}\frac{B(\nu,T)}{\tau^2}d\tau+\tau_S(\nu,\theta)\varepsilon_S(\nu,\theta)B(\nu,T_S)+\int_{\tau_S}^{1}B(\nu,T)d\tau \quad (1)$$

where $\tau_S(\nu,\theta)$ and $\tau$ are the transmittance from the surface and the model layer to the top of the atmosphere, respectively; $\varepsilon_S(\nu,\theta)$ is the surface emissivity; $T$ is the average temperature between the model layers; $T_S$ is the surface temperature; $B(\nu,T)$ represents the Planck function when the temperature is $T$.

Based on the ARMS model, the basic flow chart of AGRI infrared brightness temperature simulation with ECMWF ERA5 data as model input is shown in Figure 1. ERA5 provides atmospheric profiles for temperature, pressure and water vapor, as well as wind, surface temperature, pressure and humidity. Extract geometric variables such as longitude, latitude, satellite and solar zenith angles from AGRI data. The above atmospheric conditions and geometric variables are transformed into simulated brightness temperatures through the ARMS model. Bias properties can be assessed by comparing the difference between simulated and observed brightness temperatures.

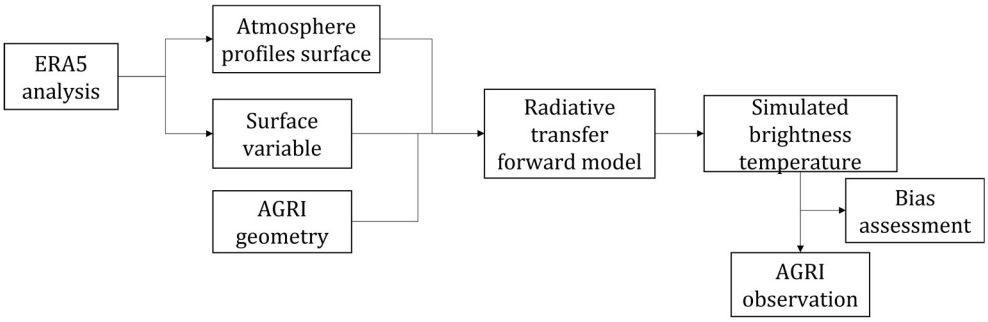


**Figure 1.** Flow chart of AGRI infrared brightness temperature simulation based on ARMS

## 3. Results and Analysis

### 3.1 Distribution of Sea-land Deviation

The brightness temperature simulated with ERA5 as data input, the spatial deviation distribution of the land surface and the ocean surface in the selected area is represented by a heat map (Fig. Hue represents a negative value, and the darker the color, the greater the deviation. Figure 2 presents the spatial distribution of brightness temperature deviations of AGRI infrared channels 8-14 over land and sea. The positive and negative deviations of AGRI infrared channel 8 are mostly in the range of 1K in the range of sea and land, and only a few areas have negative deviations of about 2K. The deviation of AGRI water vapor channel 9 in the selected area is almost all negative deviation, there is a negative deviation of 1~2K on the ocean surface, and a negative deviation of about 1K on the land surface. The situation of channel 10 and channel 9 is similar, only there is a positive deviation in the range of 1K from 30°N to 40°N. Channels 11-13 have roughly the same spatial distribution of deviations in the entire selected area, with negative deviations within 1K on the ocean surface and positive deviations within 1K on land. The deviation of channel 14 on the sea and land surfaces is almost always a positive deviation within 1K, and only some areas have a negative deviation of about 1K.

ISSN: 2414-1895 DOI: 10.6919/ICJE.202308_9(8).0021

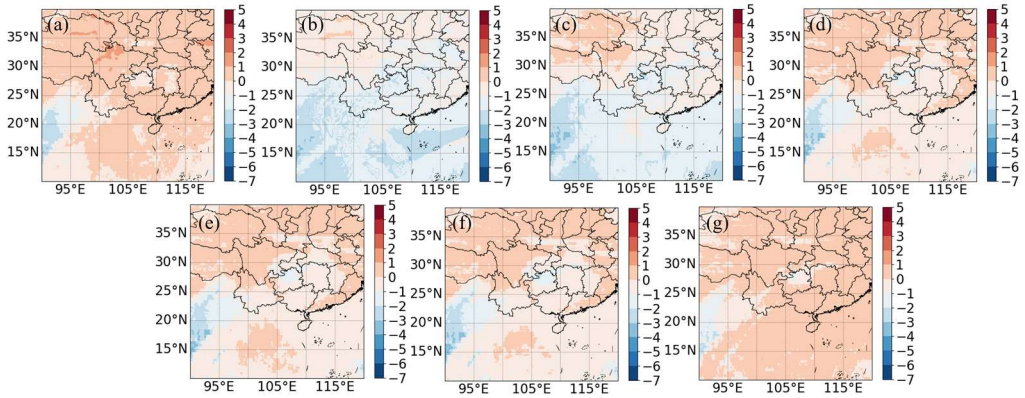


**Figure 2.** Spatial distribution of sea-land deviation of brightness temperature

Figure 3 shows the spatial mean deviation and standard deviation of the simulated brightness temperature based on Era5 data when the satellite zenith angle is less than 60°. As shown in Fig. 3(a)and(c), the positive and negative deviation trends of each channel are consistent on land and sea, that is, the deviation of near-surface channels 11-13 is negative, while the deviation of the remaining channels is positive. The largest deviations over land and ocean are at 1.34 K in channel 8 and 1.49 K in channel 14, respectively. As shown in Fig. 3(b)and(d), the standard deviation of each channel on the land is larger than that on the ocean. The standard deviation for channel 8 is highest over both land and sea, indicating that channel 8 has the most spread out distribution of deviations. Moreover, the standard deviation of channels 11-13 on the land surface is significantly higher than that of channels 9-10 and channel 14 3-4 K, and this feature is not found on the ocean. The bias and standard deviation for channels 9–10 had the smallest difference over ocean and land (the bias and standard deviation over land and ocean were less than 0.15 K and 1.2 K, respectively). The deviation and standard deviation of channels 9-10 are significantly smaller than those of other channels over land and sea, mainly due to the influence of tropospheric water vapor and temperature profiles. Over oceans and land, there is less difference in the upper and middle troposphere.

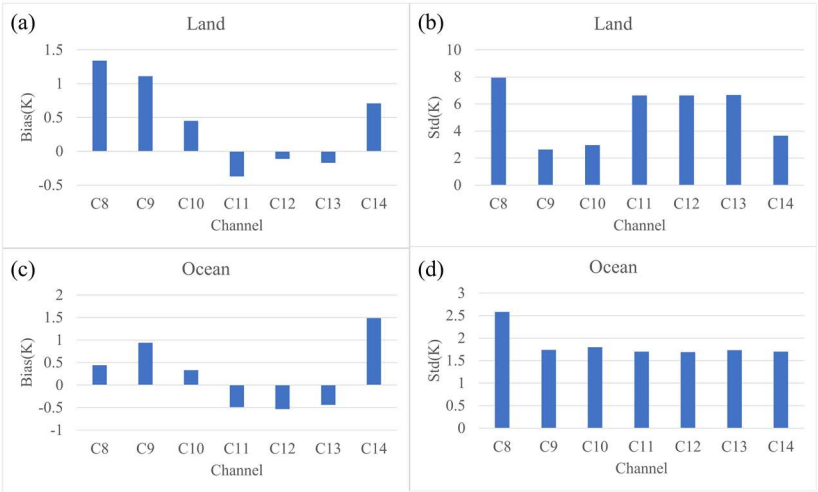


**Figure 3.** Land and Sea Deviation and Standard Deviation Statistics

## 3.2 The Effect of the satellite zenith Angle on the Deviation

Scan-related biases can be found in satellite radiation observations due to the scan pattern resulting in different scan angles within the scan line[22]. Therefore, further investigation into whether these scan-dependent biases are present in AGRI observations is warranted. Since sensor zenith angle can be converted to scan angle, scan correlation bias can be converted to the relationship between sensor zenith angle and bias. Figure 4 illustrates the variation of the bias and standard deviation with respect

ISSN: 2414-1895 DOI: 10.6919/ICJE.202308_9(8).0021

to the satellite zenith angle and the amount of data for 0.1° intervals over the ocean. The shaded part in Fig. 4(b) represents the observation counts at intervals of 0.1°. It can be seen that the number of observations with a zenith angle below 10° is small, and the observations are mainly concentrated between 10° and 60°. As can be seen in Figure 4(a), the deviations of channels 8, 10 and 11 change from negative to positive with the increase of the satellite zenith angle, and the deviation values are concentrated at 1 K, 0.5 K and 1.3 K. The deviation formula of channel 9 is positive and fluctuates around 1K. The deviation of channels 11-13 is always negative throughout the whole process, and the deviation gradually decreases with the increase of the satellite zenith angle from 0° to 20°, but after 20°, the deviation fluctuates less, maintaining at -0.5 K to -1 K between. Therefore, the satellite zenith angle has a negligible effect on the bias. As shown in the legend on the right of Fig. 4, except for channel 8, the AGRI channel deviation has no significant dependence on the satellite zenith angle. Except between 20° and 30°, the standard deviations of the 8 channels of other angles vary drastically with the satellite zenith angle. The main reason may be that channel 8 is in the mid-wave infrared band, which is more susceptible to the scattering or reflection of solar short-wave radiation in the daytime when the satellite zenith angle is large[23]. The standard deviations of the rest of the channels are concentrated in the range of 1-2 K, except that there may be small fluctuations between 20° and 30°, the fluctuations in other places are not large. The small fluctuation within 0~10° may be due to the small amount of data, which is obviously less than that in other places.

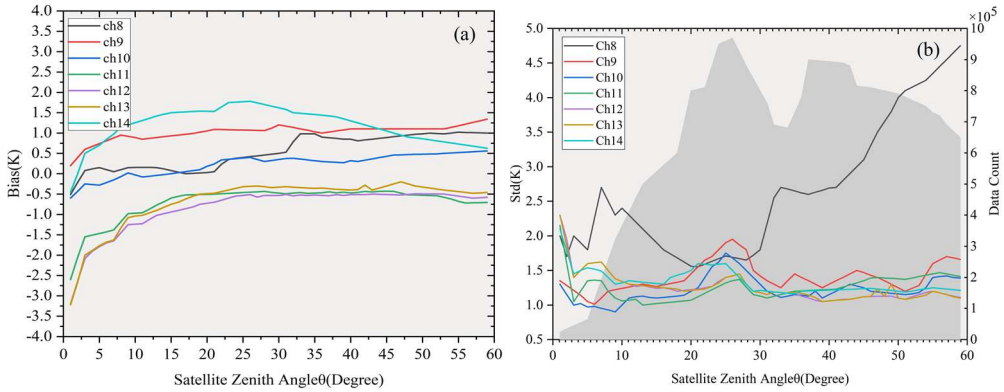


**Figure 4.** Dependence of Channels 8-14 Over the Ocean on the Satellite Zenith Angle

Figure 5 shows the dependence of the bias and standard deviation of AGRI channels 8–14 on the satellite zenith angle over land and the data counts at 0.1° intervals over land. As shown in Figure 5(a), channel 8 and channel 11 have the largest deviation changes, with deviation changes of 4 K and 4.5 K, respectively, and the deviations of the other channels are all less than 3K. All channels show positive deviation in the range of satellite zenith angle from 38° to 45°, and channels 11-13 show negative deviation in the range of 23° to 35°. As shown in Fig. 5(b), the standard deviations of channels 9, 10, and 14 are significantly smaller than those of the rest of the channels, and the peak values of the standard deviations of all channels are in the range of 35° to 40°. Comparing Figures 4 and 5, it can be found that the variation of the deviation over the land is significantly greater than that over the ocean, and the difference in standard deviation of the water vapor channels 9-10 over the ocean is greater than that over the land. On land, RTTOV surface emissivity simulates brightness temperature using a surface emissivity lookup table to generate emissivity as a function of wavenumber, latitude and longitude, and month. Therefore, the complex surface type and albedo may not be fully considered in the surface emissivity model, which may cause the sensitive channels on the surface to be affected by the observation angle when receiving radiation, while the water vapor channels 9-10 and carbon dioxide channel 14 are less affected, because this Several channels mainly receive radiation from the middle and upper troposphere.

ISSN: 2414-1895 DOI: 10.6919/ICJE.202308_9(8).0021

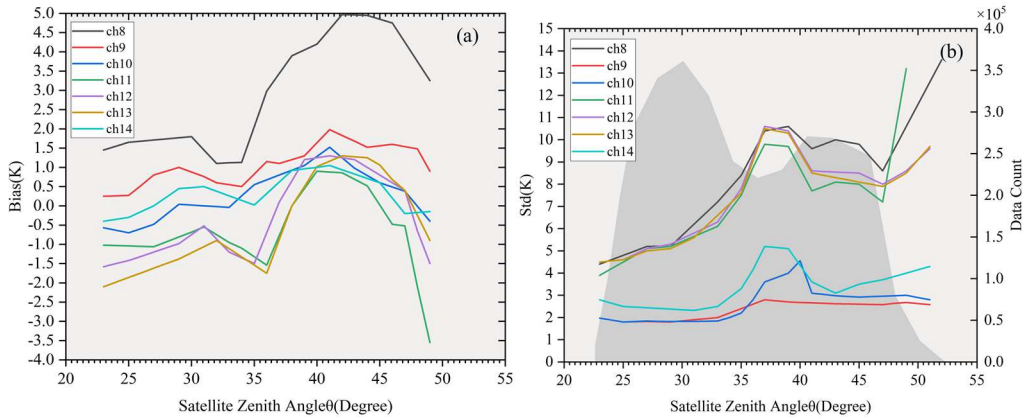


**Figure 5.** Dependence of Channels 8-14 Over the Land on the Satellite Zenith Angle

Among them, in order to quantify the correlation of all channels, this paper performs linear regression fitting between the deviation and the satellite zenith angle. Table 1 provides details on the fitted coefficients. Except channel 8 and channel 14, the fitting coefficients of other channels are all less than 0.008 K/Degree.

**Table 1.** Fitting coefficients between bias of sea-land channels 8-14 and satellite zenith angles

| Channel | Fitting coefficient | |
|---|---|---|
| | Land | Ocean |
| **8** | 0.0152 | 0.0689 |
| **9** | 0.003 | 0.0147 |
| **10** | 0.0064 | 0.0479 |
| **11** | 0.0005 | -0.0274 |
| **12** | 0.0028 | 0.0062 |
| **13** | 0.0039 | 0.0253 |
| **14** | -0.0196 | -0.0304 |

### 3.3 Influence of Observed Brightness Temperature on Bias

The heat source of the infrared imager is the black body inside the instrument, which uses space as a cold source, and the same is true for the AGRI imager, which performs self-calibration inside the instrument. Non-linear issues can cause bias in the detection of warm and cold targets, affecting the longitude of infrared imagers. Ignoring the slight nonlinearity that actually exists, assume that the imager's response to incident radiation is linear. It is necessary to further study whether these deviations show a dependence on the observed brightness temperature. Figure 6 shows the correlation coefficients and observation metrics for the observed brightness temperature value interval of 3 K and the deviation interval of 1 K. It can be seen from the figure that all channels are dependent on the observed brightness temperature, and the dependence is relatively high. In comparison, the correlation of channel 8 is lower than that of the other channels, its observation data are concentrated in 290 K~300 K, and the correlation between the deviation and the observed brightness temperature value is 0.85. The observed data of channels 9 and 10 are mostly concentrated at 240 K~260 K, and the correlations between the deviation and the observed brightness temperature are 0.91 and 0.89, respectively. The observation data of channels 11-13 are concentrated in 270 K~290 K, the distribution of observation data is generally consistent, and the correlation between the deviation and the observed brightness temperature is also relatively close, which are 0.92, 0.91 and 0.93,

ISSN: 2414-1895 DOI: 10.6919/ICJE.202308_9(8).0021

respectively. The correlation between channel 14 deviation and observed brightness temperature is the largest, reaching 0.97. The correlation of high-level channels is high, and the correlation of bottom channels is low. The possible reason is that some data problems have been corrected after recalibration, so that the observed brightness temperature value has a greater impact on the deviation.

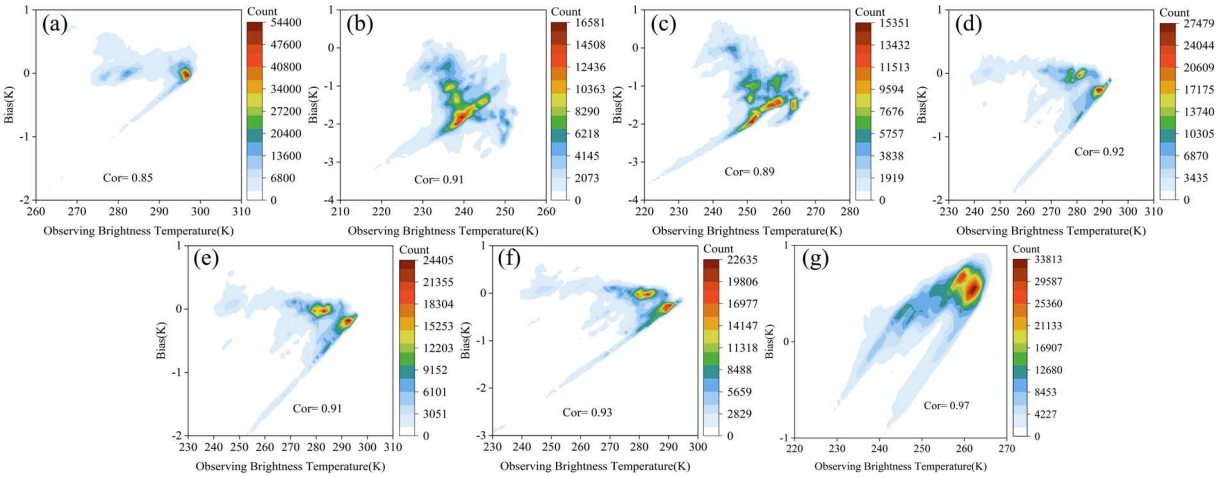


**Figure 6.** The relationship between channel 8-14 (a-g) deviation and observed brightness temperature value (Cor indicates the correlation coefficient, and the shade indicates the number of observations)

## 4. Discussions

This study preliminarily evaluates the bias characteristics of the FY-4A/AGRI infrared channel observations. There are still many uncertainties in the direct analysis of the biases, and the biases may be systematic or random. Systematic deviations may be sensor noise, behind which may be errors in sensor calibration, systematic errors in numerical prediction models, or errors in radiative transfer models. According to the study [24], the error between different models has little influence on the bias analysis because the bias statistics of different NWP fields are very similar. This means that the simulation results using other transport models are also roughly consistent with the ARMS model. It is now assumed that the robustness of the ARMS model is high, but there is an uncertainty in the estimation of the surface-sensitive channel, which is caused by the surface emission mode of the ARMS model[25]. Uncertainty can also be caused by a mismatch between the NWP model network and satellite activity trajectories, as well as by too short analysed time periods[26].

Based on the above discussion, the deviation value between land and sea, the dependence of the deviation on the satellite zenith angle and the observed brightness temperature are evaluated separately to avoid the grid mismatch error. Future research should focus on the bias correction scheme to improve the initial field accuracy and numerical forecast effect of numerical weather prediction.

## 5. Conclusion

The application of AGRI instruments has enabled China's geostationary meteorological satellite system to embark on a new journey. The high spatiotemporal and high resolution data sources obtained through AGRI scans provide great benefits for numerical weather prediction. In this study, the ARMS model was combined with the ECMWF ERA5 data to simulate the clear-sky brightness temperature of China's sea and land regions, and the deviation between the AGRI infrared channel observation data and the model simulation data was characterized. It was found that channels 8-10 and channel 14 had positive deviations, and channels 11-13 had negative deviations. Channels 11-13 have large differences in the distribution of deviations between land and sea. The deviation of the seven infrared channels on land and sea is almost within 1.5 K. On the sea surface, except for channels

ISSN: 2414-1895 DOI: 10.6919/ICJE.202308_9(8).0021

8 and 14, the correlation between the deviation of other channels and the satellite zenith angle is small, and the fitting coefficients are all less than 0.0064; while the fitting coefficients of channels 8 and 14 are 0.0152 and -0.0196, respectively. On land, the deviation of each channel has a greater correlation with the satellite zenith angle, and the fitting coefficients of each channel are larger than those on the ocean. There is a clear difference in the standard deviation of channels 8-10 and 14 and the standard deviation of channels 11-13. It was also found that all infrared channels have some dependence on the observed brightness temperature. Overall, the AGRI observations and ARMS simulations are very close.

## References

[1] Sun Hao, Wang Haoliang, Yang Jing, et al. Improving Forecast of Severe Oceanic Mesoscale Convective Systems Using FY-4A Lightning Data Assimilation with WRF-FDDA[J]. Remote Sensing. 2022,14(9): 1965-1985. DOI: 10.3390/rs14091965.

[2] Wang Gen, Wang Kefu, Han Wei, et al. Typhoon Maria Precipitation Retrieval and Evolution Based on the Infrared Brightness Temperature of the Feng-Yun 4A/Advanced Geosynchronous Radiation Imager[J]. Advances in Meteorology. 2020, 2020: 1-12.

[3] Wang Sufeng, Lu Feng, Feng Yutao. An Investigation of the Fengyun-4A/B GIIRS Performance on Temperature and Humidity Retrievals[J]. Atmosphere. 2022, 13(11): 1830-1846.

[4] Cao Dongjie, Lu Feng, Zhang Xiaohu, et al. Lightning Activity Observed by the FengYun-4A Lightning Mapping Imager[J]. Remote Sensing. 2021, 13(15): 3013-3033. DOI: 10.3390/rs13153013.

[5] Chen Xingfeng, Zhao Limin, Ding Haonan, et al. Cloud Occlusion Probability Calculation Jointly Using Himawari-8 and CloudSat Satellite Data[J]. Atmosphere. 2022, 13(11): 1754-1767.

[6] Zhao Yu, Ban Yifang. GOES-R Time Series for Early Detection of Wildfires with Deep GRU-Network[J]. Remote Sensing. 2022, 14(17): 4347-4371. DOI: 10.3390/rs14174347.

[7] Kumah K K, Maathuis B H P, Hoedjes J C B, et al. Near real-time estimation of high spatiotemporal resolution rainfall from cloud top properties of the MSG satellite and commercial microwave link rainfall intensities[J]. Atmospheric Research. 2022, 279: 106357.

[8] Letu H, Nagao T M, Nakajima T Y, et al. Ice cloud properties from Himawari-8/AHI next-generation geostationary satellite: Capability of the AHI to monitor the DC cloud generation process[J]. IEEE Transactions on Geoscience and Remote Sensing. 2018, 57(6): 3229-3239.

[9] Huang Faming, Chen Jiawu, Fan Xuanmei, et al. Logistic Regression Fitting of Rainfall-type Landslide Time Probability and Continuous Probability Landslide Hazard Modeling[J], Earth Science, 2022, 47(12): 4609-4628.

[10] Hill A J, Schumacher R S, Jirak I L. A New Paradigm for Medium-Range Severe Weather Forecasts: Probabilistic Random Forest–Based Predictions[J]. Weather and Forecasting. 2023, 38(2): 251-272.

[11] Ménégoz M, Valla E, Jourdain N C, et al. Contrasting seasonal changes in total and intense precipitation in the European Alps from 1903 to 2010[J]. Hydrology and Earth System Sciences. 2020, 24(11): 5355-5377.

[12] Bergemann M, Lane T P, Wales S, et al. High-resolution simulations of tropical island thunderstorms: Does an increase in resolution improve the representation of extreme rainfall?[J]. Quarterly Journal of the Royal Meteorological Society. 2022, 148(748): 3303-3318.

[13] Li H, Moisseev D, Luo Y, et al. Assessing Specific Differential Phase (K DP)-Based Quantitative Precipitation Estimation for the Record-Breaking Rainfall over Zhengzhou City on 20 July 2021[J]. Hydrology and Earth System Sciences. 2023, 27(5): 1033-1046.

[14] Reichle R H, Zhang S Q, Liu Q, et al. Assimilation of SMAP Brightness Temperature Observations in the GEOS Land–Atmosphere Data Assimilation System[J]. IEEE journal of selected topics in applied earth observations and remote sensing. 2021, 14: 10628-10643.

[15] Ouellet-Proulx S, Chiadjeu O C, Boucher M A, et al. Assimilation of Water Temperature and Discharge Data for Ensemble Water Temperature Forecasting[J]. Journal of Hydrology. 2017, 554: 342-359.

ISSN: 2414-1895 DOI: 10.6919/ICJE.202308_9(8).0021

[16] Yang C, Liu Z, Gao F, et al. Impact of Assimilating GOES Imager Clear-Sky Radiance with a Rapid Refresh Assimilation System for Convection-Permitting Forecast over Mexico[J]. Journal of Geophysical Research: Atmospheres. 2017, 122(10): 5472-5490.

[17] Jones T A, Wang X, Skinner P, et al. Assimilation of GOES-13 Imager Clear-Sky Water Vapor (6.5 μ m) Radiances into a Warn-on-Forecast System[J]. Monthly Weather Review. 2018, 146(4): 1077-1107.

[18] Minamide M, Zhang F. Assimilation of All-Sky Infrared Radiances from Himawari-8 and Impacts of Moisture and Hydrometer Initialization on Convection-Permitting Tropical Cyclone Prediction[J]. Monthly Weather Review. 2018, 146(10): 3241-3258.

[19] Wang Gen, Chen Qiao, Dai Juan, et al. Correction of Brightness Temperature Deviation of FY-4 Infrared Hyperspectral GIIRS MW Channel[J], Infrared, 2021, 42(05): 39-44.

[20] Newman S, Carminati F, Lawrence H, et al. Assessment of New Satellite Missions within the Framework of Numerical Weather Prediction[J]. Remote Sensing. 2020, 12(10): 1580-1595. DOI: 10.3390/rs121015 80.

[21] Gen Xiaowen, Min Jinzhong, Yang Chun, et al. Characteristic Analysis and Correction Test of FY-4A AGRI Radiation Rate Data Deviation[J], Atmospheric Science, 2020, 44(04): 679-694.

[22] Li X, Zou X, Zeng M. An Alternative Bias Correction Scheme for CrIS Data Assimilation in a Regional Model[J]. Monthly Weather Review. 2019, 147(3): 809-839.

[23] Zou X, Zhuge X, Weng F. Characterization of Bias of Advanced Himawari Imager Infrared Observations from NWP Background Simulations Using CRTM and RTTOV[J]. Journal of Atmospheric and Oceanic Technology. 2016, 33(12): 2553-2567.

[24] Newman S, Carminati F, Lawrence H, et al. Assessment of new satellite missions within the framework of numerical weather prediction[J]. Remote Sensing. 2020, 12(10): 1580-1594. DOI: 10.3390/rs12101580.

[25] Saunders R, Hocking J, Turner E, et al. An update on the RTTOV fast radiative transfer model(currently at version 12)[J]. Geoscientific Model Development. 2018, 11(7): 2717-2737.

[26] Zhu J, Shu J, Guo W. Biases characteristics assessment of the Advanced Geosynchronous Radiation Imager (AGRI) measurement on board Fengyun-4A geostationary satellite[J]. Remote Sensing. 2020, 12(18): 2871-2887. DOI: 10.3390/rs12182871.